eprints@whiterose.ac.uk
https://eprints.whiterose.ac.uk/

Terahertz quantum cascade laser with an X-valley-based injector

Mithun Roy[1] and Muhammad Anisuzzaman Talukder[1,2,a]

[1] *Department of Electrical and Electronic Engineering*

Bangladesh University of Engineering and Technology

Dhaka 1205, Bangladesh

[2] *School of Electronic and Electrical Engineering*

University of Leeds

Leeds, LS2 9JT, United Kingdom

(Dated: 26 March 2017)

We present a novel terahertz (THz) quantum cascade laser (QCL) design where Γ-valley states are used for lasing transition and X-valley states—in particular, X_z-states—are used as injector subbands. Since the lasing states in our proposed structure are populated and depopulated mainly through the interface roughness assisted Γ-X_z electron scattering, we present a model to describe this intervalley carrier transport. In the injector region of the proposed THz QCL, we use quaternary AlGaAsP material to introduce tensile strain, which plays a crucial role in increasing the gain. To compensate the strain per period, we propose to grow the periodic heterostructure on a $GaAs_{.94}P_{.06}$ virtual substrate. To simulate the carrier transport, and hence calculate the gain and lasing performance of the proposed THz QCL, we use a simplified density matrix formalism that considers resonant tunneling, dephasing, and the important intersubband scattering mechanisms. Since electron temperature significantly varies from lattice temperature for QCLs, we take their difference into account using the kinetic energy balance (KEB) method. We show that the proposed structure is capable of lasing up to a maximum lattice temperature of $\sim$119 K at 4.8 THz. For future improvements of the device, we identify major performance-degrading factors of the proposed design.

---

[a] Electronic mail: anis@eee.buet.ac.bd

I.   INTRODUCTION

Since the first realization in 2002,[1] terahertz (THz) quantum cascade lasers (QCLs) have gone through rapid improvements with respect to maximum operating temperature, output power, and frequency range covered.[2] Nevertheless, to make THz QCLs more appealing for various applications such as chemical sensing, astronomy, spectroscopy, and imaging, further improvements are necessary. In particular, high temperature operation is still an issue for THz QCLs. So far, after fifteen years of research, lasing up to $\sim$200 K has been achieved with the GaAs/AlGaAs material system,[3] while lasing up to $\sim$225 K has been achieved with the assistance of strong magnetic field.[4] Therefore, for further improvement of the temperature performance, thinking beyond the existing designs is necessary.

In QCLs based on III-V materials, carrier transfer to X-valley is often considered as an undesirable phenomenon for several reasons. Firstly, X-valley band edge is located higher in energy than Γ-valley band edge in most III-V materials used for QCL designs. Therefore, X-subbands help neither in carrier extraction from the lower lasing state (LLS) nor in carrier injection to the upper lasing state (ULS). On the contrary, X-subbands cause carrier leakage, which reduces gain and increases threshold current density.[5] Secondly, electron effective mass at X-valley is high, which discourages one to exploit X-valley states as lasing levels since gain coefficient decreases as the electron effective mass increases.[6] However, by utilizing X-valley states as injector subbands, one can expect an improved temperature performance. Since electrons prefer to scatter from a subband of lower density of states (DOS) to a subband of higher DOS, X-subbands that have higher DOS than Γ-valley states, if employed as injector states, will result in reduced thermal backfilling of the LLS.

The potential of X-valley states being used as injector subbands has inspired us to carry out this work where we design a novel THz QCL with Γ-valley states for lasing transition and X-valley states as injector subbands and investigate the performance of the designed structure. In Fig. 1, we schematically show the relevant energy levels in the Γ- and X-valleys of the proposed structure. Due to mass anisotropy and quantum confinement, electrons in X-valley can be found in non-degenerate X_z- and doubly degenerate X_{xy}-states. The intrinsic elastic $\Gamma \rightarrow X_z$ carrier scattering rate is $\sim$7 ps^{-1}, which is much greater than $\sim$0.15 ps^{-1} $\Gamma \rightarrow X_{xy}$ carrier scattering rate.[7] Therefore, we design the injector region in such a way that the carrier extraction and injection occur mainly through X_z-states. In particular, the
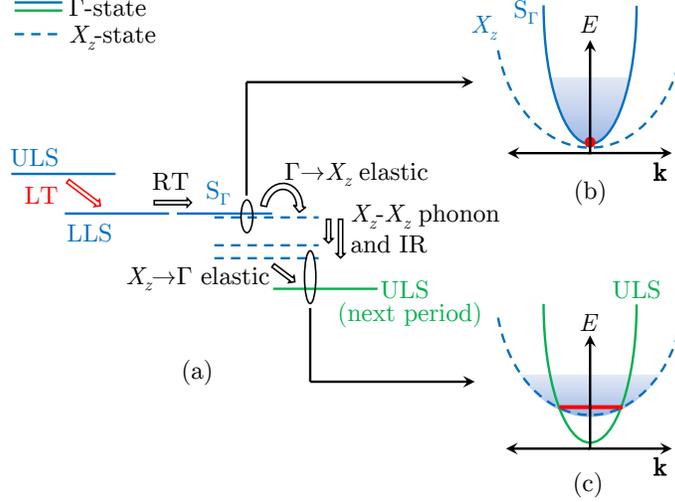
FIG. 1. Schematic illustration of (a) the energy levels in the Γ and X_z-states and carrier transport mechanisms through the energy states. Electrons scatter from a Γ-valley ULS to a Γ-valley LLS by lasing transition (LT), and then subsequently transport to another Γ-valley state S_Γ by resonant tunneling (RT). Electrons transport through X_z states in the injector region by elastic and non-elastic mechanisms. (b), (c) Energy-wave vector (E-$\mathbf{k}$) diagrams for the Γ and X_z-subbands, respectively. In both (b) and (c), electrons at the blue-shaded region can perform in-plane wave vector-non-conserving elastic transfer and those at the red region can perform in-plane wave vector-conserving elastic transfer.

carrier transport through our structure takes place according to the following sequence as shown in Fig. 1(a): First, from the LLS, electrons transfer to a Γ-state through resonant tunneling. Next, electrons are extracted from the Γ-state to a resonant injector X_z-state through $\Gamma \rightarrow X_z$ elastic scattering mechanisms. Then, carriers relax to the ground X_z-state of the injector region due to the intravalley X_z-X_z phonon and interface roughness (IR) scattering mechanisms. Finally, carriers are injected into the Γ-valley ULS of the following period from ground X_z-state mainly through the $X_z \rightarrow \Gamma$ elastic scattering mechanisms.

In semiconductor heterostructures, Γ-X_z elastic transfer can take place in two ways: With conservation of in-plane wave vector ($\mathbf{k}$) and without conservation of $\mathbf{k}$. $\mathbf{k}$-non-conserving Γ-X_z elastic transport is likely to take place due to IR assisted scattering mechanism.[7] On the contrary, if the envelope functions vary slowly compared to a sinusoid of wavelength equal to lattice parameter of the substrate, as is the case for the proposed structure, the contribution of ionized impurity scattering to the Γ-X_z transport will be small. In case of

3

$\Gamma \rightarrow X_z$ elastic scattering with the X_z-state being resonant, a small portion of the electrons of the Γ-state is allowed to perform **k**-conserving transfer, whereas all the electrons of Γ-state are eligible for the IR assisted transfer[8] as schematically shown in Fig. 1(b). This statement is also true for the $X_z \rightarrow \Gamma$ elastic scattering. Therefore, we expect that both carrier extraction and injection in our proposed structure to be dominated by the IR assisted Γ-X_z scattering mechanism as schematically shown in Fig. 1(c). Therefore, we designed the proposed structure in a way so that the IR assisted Γ-X_z scattering rate can be significant. Since IR scattering mechanism is expected to govern the Γ-X_z transfer in our design, we derive an expression to calculate the IR assisted intervalley scattering rate.

Although most of the THz QCLs to date have been realized with GaAs/AlGaAs materials, the proposed THz QCL requires novel materials for efficient carrier injection and extraction through X-valley states. In the proposed structure, we use quaternary AlGaAsP to introduce tensile strain at the injector region so that Γ and X_z quantum wells are created at the same layers. As a result, there is a significant overlap between wavefunctions of the Γ and X_z states. The significant overlap between the wavefunctions provides us an opportunity to improve the intervalley IR scattering rate. Additionally, the tensile strain places the ground X_{xy}-state at a considerably higher energy than the ground X_z-state at the injector. If the ground X_z and X_{xy} states were situated close to each other, carriers would accumulate at the injector region, and result in small gain. To ensure mechanical stability of the structure, it is necessary to compensate the strain over a period, which is done by adding 6% GaP to GaAs substrate. We calculate the average intersubband transition rates due to the dominant scattering mechanisms and use a simplified density matrix (SDM) approach to simulate the carrier transport. In addition to the Γ-X_z IR assisted transfer, in our simulation, we include the Γ-X_z phonon assisted transfer mechanism, although the scattering rate due to the latter process is weaker. Also, we consider the difference between lattice (T_{L}) and electron temperatures (T_{e}). We find that, for typical Cu metal-metal waveguide losses, our proposed THz QCL lases up to a maximum T_{L} of $\sim$119 K. Finally, we present a brief discussion on the crucial performance-degrading factors for the proposed THz QCL.

The remainder of this article is organized as follows: In Sec. II, we present a model of IR assisted Γ-X_z electron transport. In Sec. III, we present and discuss the proposed THz QCL design. In Sec. IV, we investigate the device performance and identify the major factors that are responsible for performance degradation. Finally, in Sec. V, we conclude our work

with a brief summary.

II. INTERVALLEY Γ-X_z CARRIER TRANSPORT DUE TO INTERFACE ROUGHNESS

Let us consider a heterojunction formed from two zinc-blende semiconductors with the layers grown along the [001] direction, which is the z-axis in this work. In the absence of roughness, the interface would be located at z_0. However, the fabrication process inevitably introduces imperfection at the interface, which can be described by a local deviation of the interface $\Delta(\mathbf{r})$ from z_0, where $\mathbf{r}$ denotes the two-dimensional position vector, i.e., $\mathbf{r} \equiv (x, y)$. We assume that $\Delta(\mathbf{r})$ varies continuously with $\mathbf{r}$, rather than being a discrete multiple of $a/2$, where a is the the lattice parameter of the face-centered rhombohedral cubic lattice. Interface roughness causes electrons to scatter from an initial state $\Psi_{i\mathbf{k}'} = S^{-1/2}\psi_i(z)e^{j\mathbf{k}'\cdot\mathbf{r}}\phi_i(\mathbf{R})$ with energy $E_{i\mathbf{k}'} = E_i + \hbar^2 k'^2/(2m_{ti}^*)$ to a final state $\Psi_{f\mathbf{k}''} = S^{-1/2}\psi_f(z)e^{j\mathbf{k}''\cdot\mathbf{r}}\phi_f(\mathbf{R})$ with energy $E_{f\mathbf{k}''} = E_f + \hbar^2 k''^2/(2m_{tf}^*)$. Here, subscripts i and f denote that the parameters belong to initial and final states, respectively; S denotes the in-plane cross sectional area; ψ and ϕ denote the normalized envelope function and Bloch function, respectively; j and $\mathbf{R}$ denote the imaginary unit and three-dimensional position vector, i.e., $\mathbf{R} \equiv (\mathbf{r}, z)$, respectively; $\mathbf{k}'$ and $\mathbf{k}''$ denote the in-plane wave vectors of initial and final states, respectively; E_i and E_f are the energies at the bottom of the respective subbands; and m_t^* represents the average transverse electron effective mass. Bloch functions are assumed to be real and are given by $\phi_\Gamma = u_\Gamma$, $\phi_{X_z} = e^{jQz}u_{X_z}$, where u denotes the lattice periodic part and $Q = 2\pi/a$. Additionally, we assume that u_Γ is independent of the materials that constitute the heterostructure[9] and so is u_{X_z}.

Let $U_A(\mathbf{R})$ and $U_B(\mathbf{R})$ be the crystal potentials, extended across the entire heterostructure, of the left-hand ($z < z_0$) and right-hand ($z > z_0$) materials, respectively. The deviation $\Delta(\mathbf{r})$ of the interface position produces a perturbing potential $V_p = \delta U\left[\Theta(z - z_0) - \Theta(z - z_0 - \Delta)\right]$, where $\delta U(\mathbf{R}) = U_A(\mathbf{R}) - U_B(\mathbf{R})$ and $\Theta(z)$ represents the Heaviside step function. The matrix element of V_p between initial and final states is

$$\langle \Psi_{i\mathbf{k}'}|V_p|\Psi_{f\mathbf{k}''}\rangle = \frac{1}{S}\int_S \int_{-\infty}^{\infty} \delta U \psi_i^* \psi_f P(\mathbf{R}) e^{-j(\mathbf{k}'-\mathbf{k}'')\cdot\mathbf{r}}\phi_i\phi_f \, d^2r \, dz, \tag{1}$$

where $P(\mathbf{R}) = \Theta(z - z_0) - \Theta(z - z_0 - \Delta)$. The deviation $\Delta(\mathbf{r})$ is usually small. For example,

in GaAs-based THz QCLs, the root mean square $\Delta(\mathbf{r})$ is generally smaller than the width of a monolayer of GaAs.[10] Therefore, the slowly varying envelope functions can be replaced by their values at z_0 in Eq. (1), and thus we get

$$\langle \Psi_{i\mathbf{k}'}|V_\mathrm{p}|\Psi_{f\mathbf{k}''}\rangle = \frac{1}{S}\psi_i^*(z_0)\psi_f(z_0)\int u_\Gamma \delta U u_{X_z} P(\mathbf{R})\mathrm{e}^{-\mathrm{j}(\mathbf{k}'-\mathbf{k}'')\cdot\mathbf{r}}\mathrm{e}^{\mathrm{j}Qz}\,\mathrm{d}^3R. \tag{2}$$

Since $u_\Gamma \delta U u_{X_z}$ is a lattice periodic function, we can expand it as a series using Fourier coefficients, and thereby we obtain

$$\langle \Psi_{i\mathbf{k}'}|V_\mathrm{p}|\Psi_{f\mathbf{k}''}\rangle = \frac{1}{S}\psi_i^*(z_0)\psi_f(z_0)\sum_l \widetilde{C}_l \int P(\mathbf{R})\mathrm{e}^{-\mathrm{j}(\mathbf{k}'-\mathbf{k}'')\cdot\mathbf{r}}\mathrm{e}^{\mathrm{j}Qz}\mathrm{e}^{-\mathrm{j}\mathbf{K}_l\cdot\mathbf{R}}\,\mathrm{d}^3R$$

$$= \frac{1}{S}\psi_i^*(z_0)\psi_f(z_0)\sum_l \widetilde{C}_l \widetilde{P}(\mathbf{k}'-\mathbf{k}''+\mathbf{K}_{l\|}, -Q+K_{lz}). \tag{3}$$

Here, $\mathbf{K}_l$ is the reciprocal lattice vector, $\mathbf{K}_{l\|}$ and K_{lz} are the components of $\mathbf{K}_l$ in the directions parallel and perpendicular to the layer plane, respectively, $P(\mathbf{R})$ and $\widetilde{P}(\mathbf{K})$ constitute a Fourier transform pair with $\mathbf{K}$ representing the three-dimensional wave vector [$\mathbf{K} \equiv (\mathbf{k}, K_z)$], and $\widetilde{C}_l$ denotes the Fourier series coefficient given by

$$\widetilde{C}_l = \frac{1}{\Omega_\mathrm{c}}\int_{\Omega_\mathrm{c}} u_\Gamma \delta U u_{X_z}\mathrm{e}^{\mathrm{j}\mathbf{K}_l\cdot\mathbf{R}}\,\mathrm{d}^3R$$

$$= \frac{1}{\Omega_\mathrm{c}}\int_{\Omega_\mathrm{c}} \phi_\Gamma \delta U \phi_{X_z}\mathrm{e}^{\mathrm{j}\mathbf{K}_{l\|}\cdot\mathbf{r}}\mathrm{e}^{\mathrm{j}(-Q+K_{lz})z}\,\mathrm{d}^3R, \tag{4}$$

where Ω_c is the volume of the conventional unit cell.

Now, let us consider the function $\widetilde{P}(\mathbf{K})$, which can be written as

$$\widetilde{P}(\mathbf{k}, K_z) = \left[\pi\delta(K_z) + \frac{1}{\mathrm{j}K_z}\right]\mathrm{e}^{-\mathrm{j}K_z z_0}\left[(2\pi)^2\delta(\mathbf{k}) - \int \mathrm{e}^{-\mathrm{j}K_z\Delta(\mathbf{r})}\mathrm{e}^{-\mathrm{j}\mathbf{k}\cdot\mathbf{r}}\,\mathrm{d}^2r\right]. \tag{5}$$

Using $z_0 = Na/2$ with N being a non-negative integer, expanding $\mathrm{e}^{-\mathrm{j}K_z\Delta(\mathbf{r})}$ in a power series, and utilizing the relation $K_z\delta(K_z) = 0$, we get

$$\widetilde{P}(\mathbf{k}, K_z) = \mathrm{e}^{-\mathrm{j}K_z N\frac{a}{2}}\sum_{n=1,2,3,\cdots}\frac{(-\mathrm{j}K_z)^{n-1}}{n!}\widetilde{F}_n(\mathbf{k}), \tag{6}$$

where $\widetilde{F}_n(\mathbf{k})$ and $\Delta^n(\mathbf{r})$ constitute a Fourier transform pair. In the case of intravalley Γ-Γ IR scattering, the most dominant term in the summation in Eq. (3) (in this case, $Q = 0$ and ϕ_{X_z} must be replaced by ϕ_Γ), which comes with $\mathbf{K}_0 = (0, 0, 0)$, is usually retained.[10] Likewise, in our case, we keep only the most significant terms in Eq. (3), which come with the vectors $(\mathbf{K}_{0\|}, -Q+K_{0z}) = (\mathbf{0}, -2\pi/a)$ and $(\mathbf{K}_{9\|}, -Q+K_{9z}) = (\mathbf{0}, 2\pi/a)$. The terms

6

with other vectors in the summation are less important due to smaller $|\widetilde{C}_l|$ and/or smaller $|\widetilde{P}|$. Thus, we get

$$
\begin{aligned}
\langle \Psi_{i\mathbf{k}'} | V_\mathrm{p} | \Psi_{f\mathbf{k}''} \rangle &= \frac{1}{S} \psi_i^*(z_0) \psi_f(z_0) \left[\widetilde{C}_0 \widetilde{P}(\mathbf{k}' - \mathbf{k}'', -2\pi/a) + \widetilde{C}_9 \widetilde{P}(\mathbf{k}' - \mathbf{k}'', 2\pi/a) \right] \\
&= \frac{2}{S} (-1)^N \psi_i^*(z_0) \psi_f(z_0) D \sum_{n=1,3,5,\cdots} \frac{(jQ)^{n-1}}{n!} \widetilde{F}_n(\mathbf{k}'''),
\end{aligned}
\tag{7}
$$

where $D = (1/\Omega_\mathrm{c}) \int_{\Omega_\mathrm{c}} \phi_\Gamma \delta U \phi_{X_z} \cos(2\pi z/a) \, \mathrm{d}^3 R$ and $\mathbf{k}''' = \mathbf{k}' - \mathbf{k}''$. The terms with even n vanish because they contain the integral $(1/\Omega_\mathrm{c}) \int_{\Omega_\mathrm{c}} \phi_\Gamma \delta U \phi_{X_z} \sin(2\pi z/a) \, \mathrm{d}^3 R$, which is zero. The functions $\phi_\Gamma \delta U$ and $\phi_{X_z} \sin(2\pi z/a)$ belong to Γ_1 and Γ_{15} symmetries, respectively, and hence are orthogonal. Multiplication of Eq. (7) with its complex conjugate yields

$$
|\langle \Psi_{i\mathbf{k}'} | V_\mathrm{p} | \Psi_{f\mathbf{k}''} \rangle|^2 = \frac{4}{S^2} |\psi_i(z_0)\psi_f(z_0)|^2 D^2 \sum_{n=1,3,5,\cdots} \sum_{n'=1,3,5,\cdots} \frac{(jQ)^{n+n'-2}}{n!n'!} \widetilde{F}_n(\mathbf{k}''') \widetilde{F}_{n'}^*(\mathbf{k}''').
\tag{8}
$$

Now, let us pay attention to the term $\widetilde{F}_n(\mathbf{k}''') \widetilde{F}_{n'}^*(\mathbf{k}''')$, which is given by

$$
\begin{aligned}
\widetilde{F}_n(\mathbf{k}''') \widetilde{F}_{n'}^*(\mathbf{k}''') &= S \int \left[\frac{1}{S} \int \Delta^{n'}(\mathbf{r}') \Delta^n(\mathbf{r}' + \mathbf{r}) \, \mathrm{d}^2 r' \right] e^{-j\mathbf{k}'''\cdot\mathbf{r}} \, \mathrm{d}^2 r \\
&= S \int \mathcal{E}\left[\Delta^{n'}(\mathbf{r}') \Delta^n(\mathbf{r}' + \mathbf{r}) \right] e^{-j\mathbf{k}'''\cdot\mathbf{r}} \, \mathrm{d}^2 r \\
&\equiv S \int \mathcal{E}[\Delta^{n'} \Delta_\mathbf{r}^n] e^{-j\mathbf{k}'''\cdot\mathbf{r}} \, \mathrm{d}^2 r.
\end{aligned}
\tag{9}
$$

Here, $\mathcal{E}[\cdot]$ denotes the expectation operator. We take the covariance between Δ and $\Delta_\mathbf{r}$, also known as autocovariance at lag $\mathbf{r}$, to be Gaussian. Gaussian approximation for autocovariance between Δ and $\Delta_\mathbf{r}$ is often used for modeling carrier dynamics in QCLs and has been found to agree well with experimental findings.[10] Thus, we can write

$$
\mathcal{E}[\Delta \Delta_\mathbf{r}] = \sigma^2 e^{-r^2/\Lambda^2},
\tag{10}
$$

where σ and Λ represent standard deviation and correlation length, respectively. If we further assume that $\mathcal{E}[\Delta_\mathbf{r}] = 0$ and the random vector $(\Delta, \Delta_\mathbf{r})$ has a multivariate normal distribution, we can use Isserlis theorem[11,12] to express $\mathcal{E}[\Delta^{n'} \Delta_\mathbf{r}^n]$ in terms of $\mathcal{E}[\Delta\Delta]$, $\mathcal{E}[\Delta\Delta_\mathbf{r}]$, and $\mathcal{E}[\Delta_\mathbf{r}\Delta_\mathbf{r}]$. The number of terms that need to be retained in the summation in Eq. (8) depends on a and σ. In Table I, we give expressions of $\mathcal{E}[\Delta^{n'} \Delta_\mathbf{r}^n]$ and $\widetilde{F}_n(\mathbf{k}) \widetilde{F}_{n'}^*(\mathbf{k})$, which have been found with the help of Isserlis theorem and Eq. (9), respectively, for all the pairs of (n, n') satisfying $n + n' \leq 12$. For $\sigma \leq a/6$, it is more than sufficient to retain only the

terms associated with these pairs in Eq. (8). However, additional terms may be required for larger values of σ. We note that we used $\sigma \approx a/6$ for our structure. Now, replacing $\widetilde{F}_n(\mathbf{k}''')\widetilde{F}_{n'}^*(\mathbf{k}''')$ with corresponding expressions in Eq. (8), we obtain

$$|\langle\Psi_{i\mathbf{k}'}|V_{\mathrm{p}}|\Psi_{f\mathbf{k}''}\rangle|^2 = \frac{4}{S}\pi\sigma^2\Lambda^2|\psi_i(z_0)\psi_f(z_0)|^2 D^2\bigg(M'\mathrm{e}^{-k'''^2\Lambda^2/4} + M''\mathrm{e}^{-k'''^2\Lambda^2/12}$$

$$+ M'''\mathrm{e}^{-k'''^2\Lambda^2/20} + \cdots \bigg), \tag{11}$$

where M', M'', and M''' are given by

$$M' = 1 - \frac{Q^2}{3!}6\sigma^2 + \frac{Q^4}{5!}30\sigma^4 - \frac{Q^6}{7!}210\sigma^6 + \frac{Q^8}{9!}1890\sigma^8 - \frac{Q^{10}}{11!}20790\sigma^{10} + \frac{Q^4}{3!3!}9\sigma^4$$

$$- \frac{Q^6}{3!5!}900\sigma^6 + \frac{Q^8}{3!7!}630\sigma^8 - \frac{Q^{10}}{3!9!}5670\sigma^{10} + \frac{Q^8}{5!5!}225\sigma^8 - \frac{Q^{10}}{5!7!}3150\sigma^{10} + \cdots, \tag{12a}$$

$$M'' = \frac{Q^4}{3!3!}2\sigma^4 - \frac{Q^6}{3!5!}40\sigma^6 + \frac{Q^8}{3!7!}420\sigma^8 - \frac{Q^{10}}{3!9!}5040\sigma^{10} + \frac{Q^8}{5!5!}200\sigma^8$$

$$- \frac{Q^{10}}{5!7!}4200\sigma^{10} + \cdots, \tag{12b}$$

$$M''' = \frac{Q^8}{5!5!}24\sigma^8 - \frac{Q^{10}}{5!7!}1008\sigma^{10} + \cdots. \tag{12c}$$

To find the transition rate from the initial state $\Psi_{i\mathbf{k}'}$ to all the states of the subband f, we need to apply Fermi's golden rule and then sum the result over all the wave vectors $\mathbf{k}''$. Following the steps of Ref. 10, we find the expression for the transition rate as

$$W'_{i\mathbf{k}',f} = \frac{4m^*_{\mathrm{t}f}\sigma^2\Lambda^2}{\hbar^3}|\psi_i(z_0)\psi_f(z_0)|^2 D^2\bigg[M'\int_0^\pi \mathrm{e}^{-k'''^2\Lambda^2/4}\,\Theta(k'''^2)\,\mathrm{d}\theta$$

$$+ M''\int_0^\pi \mathrm{e}^{-k'''^2\Lambda^2/12}\,\Theta(k'''^2)\,\mathrm{d}\theta + M'''\int_0^\pi \mathrm{e}^{-k'''^2\Lambda^2/20}\,\Theta(k'''^2)\,\mathrm{d}\theta + \cdots\bigg], \tag{13}$$

where $k'''(\theta)$ is given by

$$k'''(\theta) = \left[\left(1 + \frac{m^*_{\mathrm{t}f}}{m^*_{\mathrm{t}i}}\right)k'^2 + k_0^2 - 2k'\left(\frac{m^*_{\mathrm{t}f}}{m^*_{\mathrm{t}i}}k'^2 + k_0^2\right)^{1/2}\cos\theta\right]^{1/2}. \tag{14}$$

Here, $k_0^2 = 2m^*_{\mathrm{t}f}(E_i - E_f)/\hbar^2$ and θ is the angle between the wave vectors $\mathbf{k}'$ and $\mathbf{k}''$. Equation (13) represents the transition rate due to an interface located at z_0. The other interfaces, if exist, will also contribute to the scattering rate. We can assume that the standard deviations of the roughness at all the interfaces of a heterostructure are identical and so are the correlation lengths, and $\mathcal{E}[\Delta_I\Delta_{\mathbf{r},I'}] = 0$ for $I \neq I'$, where I and I' are the

8

TABLE I. The expressions of $\mathcal{E}[\Delta^{n'}\Delta_{\mathbf{r}}^{n}]$ and $\widetilde{F}_n(\mathbf{k})\widetilde{F}_{n'}^*(\mathbf{k})$ for all pairs of (n, n') that satisfy $n+n' \le$ 12.

(n, n')	$\mathcal{E}[\Delta^{n'}\Delta_{\mathbf{r}}^{n}]$	$\widetilde{F}_n(\mathbf{k})\widetilde{F}_{n'}^*(\mathbf{k})$
$(1,1)$	$\sigma^2 e^{-r^2/\Lambda^2}$	$S\pi\sigma^2\Lambda^2 e^{-k^2\Lambda^2/4}$
$(1,3),(3,1)$	$3\sigma^4 e^{-r^2/\Lambda^2}$	$S\pi 3\sigma^4\Lambda^2 e^{-k^2\Lambda^2/4}$
$(1,5),(5,1)$	$15\sigma^6 e^{-r^2/\Lambda^2}$	$S\pi 15\sigma^6\Lambda^2 e^{-k^2\Lambda^2/4}$
$(3,3)$	$9\sigma^6 e^{-r^2/\Lambda^2} + 6\sigma^6 e^{-3r^2/\Lambda^2}$	$S\pi 9\sigma^6\Lambda^2 e^{-k^2\Lambda^2/4} + S\pi 2\sigma^6\Lambda^2 e^{-k^2\Lambda^2/12}$
$(1,7),(7,1)$	$105\sigma^8 e^{-r^2/\Lambda^2}$	$S\pi 105\sigma^8\Lambda^2 e^{-k^2\Lambda^2/4}$
$(3,5),(5,3)$	$45\sigma^8 e^{-r^2/\Lambda^2} + 60\sigma^8 e^{-3r^2/\Lambda^2}$	$S\pi 45\sigma^8\Lambda^2 e^{-k^2\Lambda^2/4} + S\pi 20\sigma^8\Lambda^2 e^{-k^2\Lambda^2/12}$
$(1,9),(9,1)$	$945\sigma^{10} e^{-r^2/\Lambda^2}$	$S\pi 945\sigma^{10}\Lambda^2 e^{-k^2\Lambda^2/4}$
$(3,7),(7,3)$	$315\sigma^{10} e^{-r^2/\Lambda^2} + 630\sigma^{10} e^{-3r^2/\Lambda^2}$	$S\pi 315\sigma^{10}\Lambda^2 e^{-k^2\Lambda^2/4} + S\pi 210\sigma^{10}\Lambda^2 e^{-k^2\Lambda^2/12}$
$(5,5)$	$225\sigma^{10} e^{-r^2/\Lambda^2} + 600\sigma^{10} e^{-3r^2/\Lambda^2}$ $+120\sigma^{10} e^{-5r^2/\Lambda^2}$	$S\pi 225\sigma^{10}\Lambda^2 e^{-k^2\Lambda^2/4} + S\pi 200\sigma^{10}\Lambda^2 e^{-k^2\Lambda^2/12}$ $+S\pi 24\sigma^{10}\Lambda^2 e^{-k^2\Lambda^2/20}$
$(1,11),(11,1)$	$10395\sigma^{12} e^{-r^2/\Lambda^2}$	$S\pi 10395\sigma^{12}\Lambda^2 e^{-k^2\Lambda^2/4}$
$(3,9),(9,3)$	$2835\sigma^{12} e^{-r^2/\Lambda^2} + 7560\sigma^{12} e^{-3r^2/\Lambda^2}$	$S\pi 2835\sigma^{12}\Lambda^2 e^{-k^2\Lambda^2/4} + S\pi 2520\sigma^{12}\Lambda^2 e^{-k^2\Lambda^2/12}$
$(5,7),(7,5)$	$1575\sigma^{12} e^{-r^2/\Lambda^2} + 6300\sigma^{12} e^{-3r^2/\Lambda^2}$ $+2520\sigma^{12} e^{-5r^2/\Lambda^2}$	$S\pi 1575\sigma^{12}\Lambda^2 e^{-k^2\Lambda^2/4} + S\pi 2100\sigma^{12}\Lambda^2 e^{-k^2\Lambda^2/12}$ $+S\pi 504\sigma^{12}\Lambda^2 e^{-k^2\Lambda^2/20}$

interface indices.[10] Thus, the total transition rate becomes

$$
W_{i\mathbf{k}',f} = \frac{4m_{\text{t}f}^*\sigma^2\Lambda^2}{\hbar^3}\left[\sum_I |\psi_i(z_I)\psi_f(z_I)|^2 D_I^2\right]\left[M'\int_0^\pi e^{-k'''^2\Lambda^2/4}\,\Theta(k'''^2)\,\mathrm{d}\theta\right.
$$

$$
\left. + M''\int_0^\pi e^{-k'''^2\Lambda^2/12}\,\Theta(k'''^2)\,\mathrm{d}\theta + M'''\int_0^\pi e^{-k'''^2\Lambda^2/20}\,\Theta(k'''^2)\,\mathrm{d}\theta + \cdots\right]. \quad (15)
$$

The expression of D in its original form is not convenient for the design purpose because it does not explicitly show how D varies with the known material parameters, e.g., band offset. Therefore, we examine whether D can be expressed in a convenient form. The Bloch functions at the Γ-point are complete with respect to lattice periodic functions.[13] The function $\phi_{X_z}\cos(2\pi z/a)$, being lattice periodic, can be expressed as a linear combination of the Γ Bloch functions, i.e.,

$$
\phi_{X_z,1}\cos(2\pi z/a) = \sum_s c_s u_{\Gamma,s}\,, \quad (16)
$$

where c stands for the numerical coefficient, s stands for the band index, i.e., $s = 0, 1, 2, \cdots$, and the band corresponding to $s = 1$ is taken as the conduction band. We note that the band index was not shown explicitly in the previous calculations as the involved quantities belonged to only one band, i.e., conduction band. Using AlAs Bloch functions given in Ref. 14, we find $|c_1| \approx 0.5$. GaAs Bloch functions[14] also yield an approximately identical value. Now, let us find D for a GaAs/AlAs heterostructure. Since we used GaAs$_{.94}$P$_{.06}$ as the virtual substrate in our structure, we assume that every heterostructure considered in this section for the calculation of D is pseudomorphically grown on GaAs$_{.94}$P$_{.06}$. Using AlAs Bloch functions in the calculations, we can write

$$
\begin{aligned}
D_{\text{GaAs/AlAs}} &= \frac{1}{\Omega_{\text{c}}} \int_{\Omega_{\text{c}}} u_{\Gamma,1,\text{AlAs}}(U_{\text{GaAs}} - U_{\text{AlAs}})\phi_{X_z,1,\text{AlAs}} \cos(2\pi z/a)\, \mathrm{d}^3 R \\
&= \frac{1}{\Omega_{\text{c}}} \int_{\Omega_{\text{c}}} u_{\Gamma,1,\text{AlAs}}(H_{\text{GaAs}} - H_{\text{AlAs}}) \sum_s c_{s,\text{AlAs}}\, u_{\Gamma,s,\text{AlAs}}\, \mathrm{d}^3 R,
\end{aligned} \tag{17}
$$

where H denotes the Hamiltonian operator. If we assume that $\int_{\Omega_{\text{c}}} u_{\Gamma,1,\text{AlAs}} H_{\text{GaAs}}\, u_{\Gamma,s,\text{AlAs}}\, \mathrm{d}^3 R \approx 0$ for $s \neq 1$ due to orthogonality, Eq. (17) simplifies to

$$
|D_{\text{GaAs/AlAs}}| \approx |c_{1,\text{AlAs}}|V_{\text{GaAs/AlAs}}^{\Gamma} \approx \frac{V_{\text{GaAs/AlAs}}^{\Gamma}}{2}, \tag{18}
$$

where V^{Γ} represents the Γ-valley conduction band offset. To justify the orthogonality assumption, we also directly calculate $D_{\text{GaAs/AlAs}}$ using the pseudopotential form factors of GaAs and AlAs given in Ref. 15. We note that, for a GaAs/AlAs heterostructure grown on GaAs$_{.94}$P$_{.06}$, the Γ-band offset is $\sim$958 meV. Therefore, we take the form factor $V^{\text{S}}(0)$ of AlAs to be -0.457 eV so that the Γ-valley conduction band offset becomes $\sim$958 meV, i.e., $|(1/\Omega_{\text{c}}) \int_{\Omega_{\text{c}}} u_{\Gamma,1,\text{AlAs}}(U_{\text{AlAs}} - U_{\text{GaAs}})\, u_{\Gamma,1,\text{AlAs}}\, \mathrm{d}^3 R| \approx 958$ meV. We find that $|D_{\text{GaAs/AlAs}}| \approx V_{\text{GaAs/AlAs}}^{\Gamma}/4$, which proves that Eq. (18) cannot be true for the proposed structure and the orthogonality of the states cannot be assumed. Now, consider an Al$_m$Ga$_{1-m}$As/Al$_{m'}$Ga$_{1-m'}$As structure. If we apply linear interpolation scheme to find the form factors of ternary AlGaAs, we get $|D_{\text{Al}_m\text{Ga}_{1-m}\text{As}/\text{Al}_{m'}\text{Ga}_{1-m'}\text{As}}| = |(m-m')D_{\text{GaAs/AlAs}}| \approx |m-m'|V_{\text{GaAs/AlAs}}^{\Gamma}/4 = V_{\text{Al}_m\text{Ga}_{1-m}\text{As}/\text{Al}_{m'}\text{Ga}_{1-m'}\text{As}}^{\Gamma}/4$ for any m and m'.

Now, let us calculate D for the Al$_{.10}$Ga$_{.90}$As$_{.68}$P$_{.32}$/AlAs heterostructure. As the mole fraction of aluminum is small, we assume the form factors of quaternary Al$_{.10}$Ga$_{.90}$As$_{.68}$P$_{.32}$ to be equal to those of ternary GaAs$_{.68}$P$_{.32}$. We find the form factors of GaAs$_{.68}$P$_{.32}$ by linearly interpolating those of GaP[16] and GaAs. We note that the Γ-band offset is

10

$\sim$748 meV for this heterostructure, which is assumed to be grown on $GaAs_{.94}P_{.06}$ substrate. Therefore, we take the form factor $V^S(0)$ of $GaAs_{.68}P_{.32}$ as -0.039 eV so that $|(1/\Omega_c) \int_{\Omega_c} u_{\Gamma,1,AlAs}(U_{AlAs} - U_{Al_{.10}Ga_{.90}As_{.68}P_{.32}}) u_{\Gamma,1,AlAs} \, d^3R| \approx 748$ meV. Therefore, the calculation results in $|D_{Al_{.10}Ga_{.90}As_{.68}P_{.32}/AlAs}| \approx V^{\Gamma}_{Al_{.10}Ga_{.90}As_{.68}P_{.32}/AlAs}/4$. For $Al_{.10}Ga_{.90}As_{.68}P_{.32}$ /$Al_{.68}Ga_{.32}As$ heterostructure, we get a similar result as well. Therefore, we conclude that D, for a heterojunction that matches closely to one of the categories discussed above, can be expressed as

$$|D| \approx \frac{V^{\Gamma}}{4} \, . \tag{19}$$

We emphasize that Eq. (19) is an approximate one as we have not taken into account complexities such as bowing and strain induced modification of the pseudopotential form factors. In this paper, we use Eq. (15) with D as given by Eq. (19) to calculate the intervalley IR scattering rate. In Eq. (15), we include only M', M'', and M''' terms and neglect higher order terms, and in Eqs. (12a)–(12c), we include terms up to Q^{10} and neglect higher order terms.

To validate the developed model, we have calculated $\Gamma \rightarrow X_z$ scattering lifetime for a GaAs/AlAs multiple-quantum-well structure that has been investigated experimentally in Ref. 17. The investigated structure consists of 100 alternating layers of 10-nm-thick GaAs quantum wells and 2.5-nm-thick AlAs barriers. Intervalley electron scattering time from the second Γ-miniband to the first X_z-miniband was experimentally determined as 2.5 ps at $T_L = 10$ K. With the help of Eqs. (15) and (19), we calculated the same scattering lifetime for this structure and found it to be 3.15 ps. This close agreement between the theoretical and experimental values validates our model. In this calculation, we have set $T_e = T_L + 100$ K. We have also used $\sigma = 0.94$ Å and $\Lambda = 100$ Å, which are within the ranges that are often used for the GaAs-based THz QCLs.[10]. We note that the uncertainty in the parameter values can play a role in the difference between the calculated and experimental values.

III. DEVICE DESIGN

The key feature of the proposed THz QCL structure is the X-valley-based injector region. Therefore, it is important to discuss the principle that we followed in designing the injector region. Before we present the proposed structure, we show what we may expect if we use AlGaAs and AlAs materials for a THz QCL with an X-valley based injector
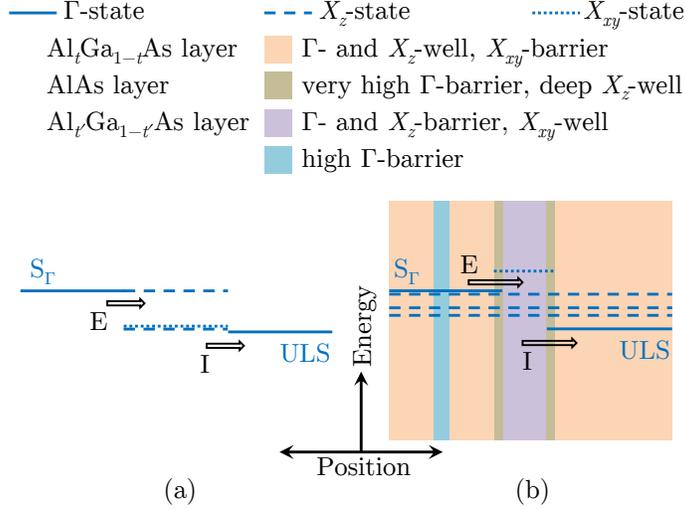
11

FIG. 2. Schematic illustration of the layers and localization of the wavefunctions for the injector regions of QCLs that exploit X_z-states for carrier extraction (E) and injection (I). The horizontal blue colored solid, dashed, and dotted lines are used to indicate the regions where the envelope functions of respectively the Γ-, X_z-, and X_{xy}-states are mostly concentrated. The injector region in (a) belongs to a typical AlGaAs/AlAs-based QCL, whereas the injector region in (b) belongs to the proposed design. In both (a) and (b), carriers transfer from LLS (not shown) to S_{Γ}-state through RT, subsequently scatter to the X_z-states due to IR, and finally reach the ULS from the ground X_z-state through the intervalley IR scattering mechanism. The AlGaAs/AlAs-based injector region in (a) is assumed to be designed in a way so that the spread of the envelope functions of the lasing states and the lasing frequency are approximately identical to that in (b).

region. Figure 2(a) schematically illustrates the layers and localization of the wavefunctions for the injector region of a typical AlGaAs/AlAs-based QCL—assumed to be grown on GaAs substrate—that employs X_z-states as injector subbands. The major drawback of AlGaAs/AlAs-based structures is that the ground X_{xy}-state is located in energy very close to the ground X_z-state in the AlAs layer. Since the $X_{xy} \to \Gamma$ IR scattering rate is very slow, the total out-scattering rate is much smaller than the total in-scattering rate for the X_{xy}-state. As a result, a significant number of carriers accumulate at X_{xy}-state, causing the current density (J) to be small. Due to a small J, this type of structures will yield a small gain.

However, we can overcome the carrier accumulation at X_{xy} by using a design principle as is schematically shown in Fig. 2(b). In this scheme, the orange layers will serve as quantum

wells for both the Γ- and X_z-valleys and as barriers for the X_{xy}-valley. The thicknesses of the X_z-wells, i.e., orange layers, will be chosen in a way so that the corresponding X_z-states extend over the wells, as shown by the blue dashed lines. The thinnest two tan layers will help to enhance the intervalley IR scattering rate in two ways: Firstly, the deep X_z-wells attract the X_z envelope functions and thus increase their absolute values at the interfaces; secondly, they introduce very high Γ-band offsets. This new scheme has two advantages over the AlGaAs/AlAs-based structures. Firstly, the ground X_{xy}-state is located significantly above the ground X_z-state as the orange layers act as barriers to the X_{xy}-valley, and hence barely affects the gain unlike the previous structure. Secondly, in this design, a significant overlap occurs between the X_z- and Γ-wavefunctions, i.e., between the wavefunctions of S_Γ and ULS, which allows us to further enhance the intervalley IR scattering rate. In particular, this scheme offers substantial amount of space containing significant values (magnitudes) of both the Γ and X_z envelope functions, and within that region, we may insert thin layers of a material with a high Γ-band edge. As Fig. 2(b) shows, a thin aqua layer with high Γ-band edge will be inserted at the overlapping region of the envelope functions of S_Γ and X_z-states, to enhance the carrier extraction rate. To improve the extraction or injection rates even further, a number of such layers can be inserted in the orange layers.

Following the principle outlined in Fig. 2(b), we designed a THz QCL structure. The thicknesses and material compositions of different layers of the structure are given in Table II. We use AlGaAsP with the mole fractions specified in Table II to introduce tensile strain in the corresponding layers. The in-plane tensile strain lowers both the Γ- and X_z-band edges in layers L1, L7, and L9 compared to when the layers are not strained, and thereby forms quantum wells, as shown in Fig. 3. As a result, a considerable overlap occurs between the Γ- and X_z-wavefunctions. The tensile strain also elevates the X_{xy}-band edge in the same L1, L7, and L9 layers, as is also shown in Fig. 3. As a result, the ground X_{xy}-state, which is mostly concentrated in the layers L10, L11, and L12, is located substantially higher in energy than the ground X_z-state.

To ensure mechanical stability, the thicknesses of individual strained layers must be kept within a limit known as critical layer thickness (CLT). People's and Bean's energy balance model[18] and Matthews' and Blakeslee's mechanical equilibrium model[19] are the two most popular methods to determine CLT. However, it has been shown in different literatures[18,20,21] that Matthews' and Blakeslee's model often underestimates the critical thickness. Therefore,

TABLE II. Material composition, thickness, and amount of in-plane strain ($\epsilon_\parallel$) for each of the layers of a period of our designed THz QCL. The values of $\epsilon_\parallel$ were calculated by assuming that the structure was grown on a virtual substrate $GaAs_{.94}P_{.06}$. Positive (negative) sign before $\epsilon_\parallel$ implies that the corresponding layer is under tensile (compressive) strain. Layers are labeled from L1 to L12.

Layer	Material used	Thickness (Å)	$\epsilon_\parallel$ (%)	Layer	Material used	Thickness (Å)	$\epsilon_\parallel$ (%)
L1	$Al_{.13}Ga_{.87}As_{.71}P_{.29}$	45	+0.81	L7	$Al_{.10}Ga_{.90}As_{.68}P_{.32}$	17	+0.92
L2	$Al_{.27}Ga_{.73}As$	23	−0.25	L8	$Al_{.68}Ga_{.32}As$	06	−0.31
L3	$Al_{.43}Ga_{.57}As$	23	−0.28	L9	$Al_{.10}Ga_{.90}As_{.68}P_{.32}$	17	+0.92
L4	$Al_{.29}Ga_{.71}As$	76	−0.26	L10	AlAs	03	−0.36
L5	$Al_{.43}Ga_{.57}As$	62	−0.28	L11	$Al_{.43}Ga_{.57}As$	17	−0.28
L6	$Al_{.27}Ga_{.73}As$	20	−0.25	L12	AlAs	03	−0.36

in this work, we use People's and Bean's model to calculate CLTs of different strained layers. With the help of People's and Bean's model, the CLT for layers L7 and L9, which are under the highest strain according to Table II, is determined as ~1458 Å. Because of smaller strain, the CLTs of other layers are much greater than 1458 Å. Table II shows that the layer thicknesses of the designed structure are well within the limit limit of CLT. Furthermore, according to the strain balancing model,[22] the lattice parameter of the substrate should be 5.6391 Å to completely compensate the strain over a period. We chose $GaAs_{.94}P_{.06}$ as the virtual substrate, which has a lattice parameter $\approx$ 5.641 Å for the growth of periodic quantum heterostructure. With $GaAs_{.94}P_{.06}$ as the virtual substrate, the net strain per period can be calculated as ~0.03%, which is so small that one can assume the structure to be strain balanced.

The unstrained conduction band offsets for relevant ternary semiconductors were derived with the help of valence band offsets, band gaps, and bowing parameters. The relations for Γ- and X-valley band offsets are shown in Table III. The necessary data were collected from Refs. 23 and 24. The material parameters necessary to determine strain-splitting and to solve Schrödinger and Poisson equations are listed in Table IV. The Γ-valley effective masses for relevant binaries and ternaries were calculated following an approach discussed
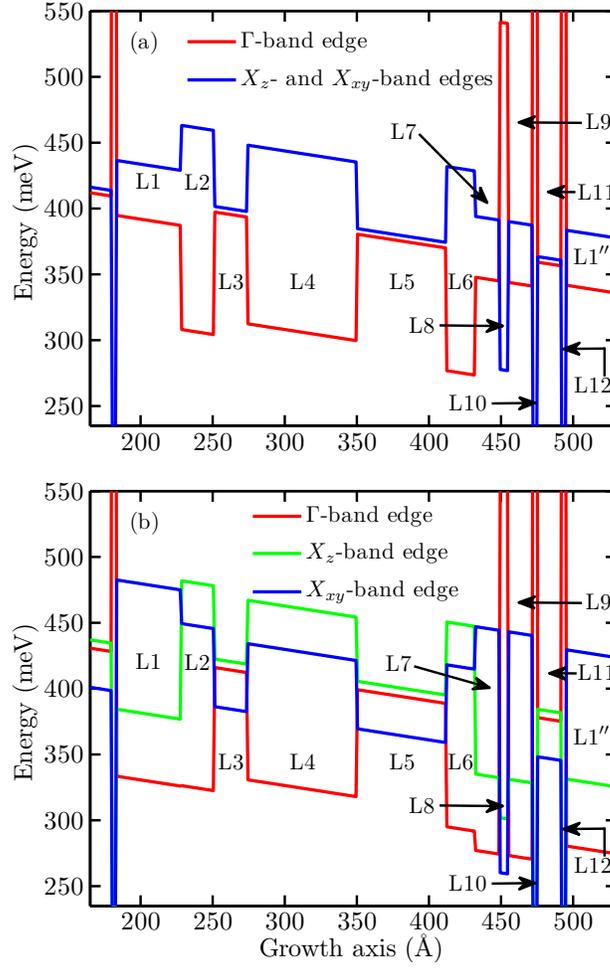
FIG. 3. Potential profiles for a period of the designed QCL in (a) unstrained and (b) strained conditions at 17 kV/cm bias. The details of the layers are given in Table II. Layers L1 and L1″ mark the beginning of the respective periods.

TABLE III. Unstrained Γ- and X-valley conduction band offsets for different ternary semiconductors relevant to this work. The band offsets were calculated with respect to the Γ-valley conduction band edge of GaAs.

Ternary material	Γ-valley band offset (meV)	X-valley band offset (meV)
$Al_rGa_{1-r}As$	$1136.7r - 1492r^2 + 1310r^3$	$476.3 - 360.6r$
$AlAs_{1-r}P_r$	$954.7 - 80.3r + 220r^2$	$115.7 - 306.3r + 220r^2$
$Al_rGa_{1-r}P$	$788.7 + 305.7r$	$284.4 - 384.9r + 130r^2$
$GaAs_rP_{1-r}$	$788.7 - 978.7r + 190r^2$	$284.4 - 48r + 240r^2$

15

TABLE IV. Lattice parameters, effective masses at Γ-valley (m^{Γ}) at 98 K, longitudinal and transverse effective masses at X-valley (m^{l} and m^{t}, respectively), elastic stiffness constants (C_{11}, C_{12}), static and high frequency dielectric constants ($\varepsilon_{\mathrm{r0}}$ and $\varepsilon_{\mathrm{r\infty}}$, respectively), hydrostatic deformation potentials at Γ- and X-valleys (a_{h}^{Γ} and a_{h}^{X}, respectively), and shear deformation potentials at X-valley (a_{s}^{X}) for different binary semiconductors relevant to our work.[23,27–31] m_0 denotes the rest mass of a free electron.

Material	a	m^{Γ}	m^{l}	m^{t}	C_{11} ($\times10^{11}$	C_{12} ($\times10^{11}$	$\varepsilon_{\mathrm{r0}}$	$\varepsilon_{\mathrm{r\infty}}$	a_{h}^{Γ}	a_{h}^{X}	a_{s}^{X}
	(Å)	($\times m_0$)	($\times m_0$)	($\times m_0$)	dyn/cm^2)	dyn/cm^2)			(eV)	(eV)	(eV)
GaAs	5.65325	0.066	0.741	0.230	11.84	5.370	12.90	10.86	-7.17	1.05	6.50
AlAs	5.66110	0.150	0.741	0.284	11.93	5.730	10.06	08.16	-5.64	1.20	6.90
GaP	5.45050	0.129	3.060	0.253	14.05	6.203	11.00	08.80	-7.14	2.70	6.30
AlP	5.46720	0.219	0.900	0.300	13.25	6.670	09.60	07.40	-5.54	1.81	3.25

in Ref. 23. To estimate the other material parameters for ternaries, linear interpolation scheme was adopted. It is well-known that the X-valley dispersions of bulk AlAs and GaP take the form of a "camel's back."[25,26] Therefore, to find m^{l} for AlAs and GaP, we used[26]

$$m^{\mathrm{l}} = m_z \left[1 - \left(\frac{\zeta}{\zeta_0} \right)^2 \right]^{-1}, \tag{20}$$

where m_z is the effective mass in the z-direction in the absence of interaction between the X_1 and X_3 bands, ζ is the energy difference between the bulk X_1 and X_3 states, $\zeta_0 = 2m_z R^2/\hbar^2$, and R is a band parameter. The camel's back parameters for AlAs and GaP were collected from Refs. 25 and 32, respectively. GaAs was assumed to have the camel's back dispersion with the parameters identical to those of AlAs.[33] In the case of AlP, camel's back dispersion was not assumed and the value presented in Ref. 31 was used for m^{l}. To approximate the conduction band offsets, as well as other material parameters for quaternary AlGaAsP, the interpolation method introduced by Glisson et al.[34] was used.

By solving the Schrödinger equation separately for Γ- and X_z-potential profiles in the effective mass approximation, we found the envelope functions, which are shown in Fig. 4. The non-parabolic dispersion around the Γ-point was taken into consideration by assuming the effective mass to be energy dependent.[35] We doped layer L6 and the adjacent-half of layer L5 with Si to have a total electron sheet density of 2.7×10^{10} cm^{-2} under complete
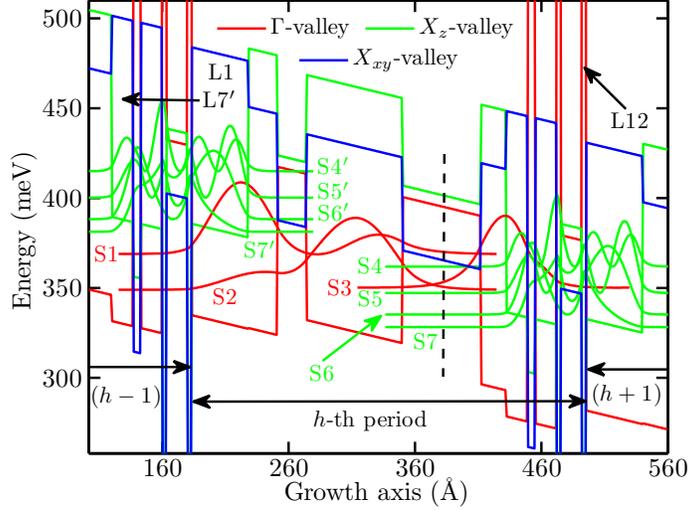
FIG. 4. Potential profile along with moduli-squared envelope functions of the designed THz QCL at an applied electric field of 17 kV/cm and an operating temperature of 98 K. Here, h stands for the period index. States S1 to S7 and S1$'$ to S7$'$ belong to the h-th and $(h-1)$-th periods, respectively. S1 and S2 act as the ULS and LLS, respectively. The X_{xy}-states are not shown as they play a minor role in carrier transport.

ionization. We also solved the Poisson equation and found the maximum band-bending to be $\sim$1.5 meV only, and hence, neglected the potential due to space charge. Our calculation shows that, at the design bias of 17 kV/cm and temperature of 98 K, the energy difference between the ULS and LLS becomes equivalent to an emission frequency of $\sim$4.8 THz.

In our proposed THz QCL, carriers scatter from the X_z-states, predominantly from S7$'$, of the $(h-1)$-th period to the ULS of the h-th period mainly due to IR. We used AlAs for layer L12$'$, which provides a high Γ-band offset as well as a deep X_z-well, and thus enhances the IR assisted $X_z \rightarrow \Gamma$ scattering rate. Because the DOS associated with an X_z-subband is higher, the back-scattering of carriers from S1 to S7$'$ would be significant if the two states were resonant. So, S1 state was designed to be situated $\sim$12 meV lower in energy than S7$'$. Layers L2 and L6$'$ were used to restrict the X_z-wells from being very wide. Replacing the materials of the above layers with those of respectively L1 and L7$'$—thus making the X_z-wells as wide as the corresponding Γ-wells—we found that the gain dropped. This happened mainly due to the decrease in the average $X_z \rightarrow$ ULS IR scattering rate, which ensued from the attenuation of the X_z envelope functions at the interfaces of L12$'$, which results due to widening the X_z-wells.

17

From LLS, carriers move to state S3 through resonant tunneling. In the designed structure, the anticrossing energy gap for the doublet S2↔S3 was made ~4.8 meV. From state S3, carriers scatter to X_z-states—predominantly to the resonant state S5—of the h-th period through mainly the intervalley IR scattering. Layer L10 enhances the $\Gamma \to X_z$ IR scattering rate in the same manner layer L12′ does for the $X_z \to \Gamma$ transfer. Because both L7 and L9 serve as quantum wells for both the Γ- and X_z-valleys, considerable overlap occurs between the envelope functions of S3 and the X_z-states, and this situation allowed us to further enhance the IR scattering rate. As is shown in Fig. 4, we inserted a thin layer L8 of high Γ-band edge at the region where the envelope functions of the states from both the valleys have significant magnitudes, thereby improving the scattering rate. Finally, from the states S4 and S5, carriers move to the lower states through the intravalley longitudinal optical (LO) phonon and IR scattering mechanisms.

IV.   PERFORMANCE EVALUATION AND DISCUSSION

For the simulation of carrier transport, we used an SDM formalism.[10] In the carrier transport model, we included intravalley LO[22] and intervalley X-point phonon scattering,[5] and inter- and intravalley[10] IR scattering mechanisms. Since layer L4 is the widest Γ-well in the structure, the energy of the LO phonons responsible for the Γ-Γ carrier-phonon scattering was assumed to be equal to the energy of the LO phonons of $Al_{.29}Ga_{.71}As$, which forms L4. For the ternary AlGaAs, the energy of the GaAs-like LO phonon was calculated according to Ref. 36. Since the envelope functions of the injector X_z-states are mostly concentrated in the AlGaAsP layers and layer L1 is the widest of them, we assumed the LO phonons for the carrier-phonon scattering between the X_z-states to have energy equal to that of the LO phonons of $Al_{.13}Ga_{.87}As_{.71}P_{.29}$. Because $Al_{.13}Ga_{.87}As$ and $GaAs_{.71}P_{.29}$ are dominating among all the four ternaries of which the quaternary $Al_{.13}Ga_{.87}As_{.71}P_{.29}$ is composed and the energies of the GaAs-like LO phonons are expected to be nearly identical in these two ternaries. We note that Ref. 37 experimentally determined the energy of the GaAs-like LO phonons of $GaAs_{.77}P_{.23}$, which is very close to that of the GaAs-like LO phonons of $Al_{.13}Ga_{.87}As$. Since the difference in the mole fractions of $GaAs_{.77}P_{.23}$ and $GaAs_{.71}P_{.29}$ is small, we expect the GaAs-like LO phonons of $GaAs_{.71}P_{.29}$ also to be equal in energy to that of $Al_{.13}Ga_{.87}As$. The GaAs-like LO phonons of $Al_{.13}Ga_{.87}As_{.71}P_{.29}$ were taken to be equal in

TABLE V. Average phonon and IR assisted carrier scattering rates between relevant states and electron sheet densities at 17 kV/cm bias and 98 K temperature. State S1″ belongs to the $(h+1)$-th period.

Average scattering rates			Subband populations	
States involved	Phonon	IR	State	Population
	$(\times 10^{12}\ \text{s}^{-1})$	$(\times 10^{12}\ \text{s}^{-1})$		$(\times 10^{9}\ \text{cm}^{-2})$
S1 → S2, S2 → S1	0.63, 0.05	0.06, 0.01	S1	5.39
(S3 → S4) + (S3 → S5) (carrier extraction)	0.05	1.93	S2	2.80
S5 → S3	0.01	0.35	S3	1.97
(S4 → S6) + (S4 → S7)	3.51	1.28	S4	0.39
(S5 → S6) + (S5 → S7)	0.97	3.94	S5	1.62
S6 → S5, S7 → S5	0.08, 0.05	0.47, 0.33	S6	4.85
Average carrier injection from X_z-states to S1″	0.07	0.30	S7	9.98
Total backscattering from S1″ to X_z-states	0.05	0.37		

energy to that of $Al_{.13}Ga_{.87}As$. The intervalley Γ-X_z carrier-phonon scattering was supposed to be caused by the X-point longitudinal acoustic (LA) phonons of $Al_{.13}Ga_{.87}As_{.71}P_{.29}$. The X-point LA phonons in GaAs have X_1 symmetry.[27] As $Al_{.13}Ga_{.87}As_{.71}P_{.29}$ is rich in GaAs, the X-point LA phonons in this quaternary are expected to have X_1 symmetry. The X-point LA phonon energy was calculated according to the interpolation scheme of Glisson $et\ al.$[34] The LA phonon energies for the binaries GaAs, AlAs, GaP, and AlP were taken as 27.9,[38] 42.3,[27] 31,[39] and 43.9 meV,[40] respectively. The intervalley Γ-X deformation potential constant was taken to be the same as that of GaAs.[41] For both the inter- and intravalley IR scattering, we used $\sigma = 0.94$ Å, which yields $\sigma \approx a/6$, where $a \approx 5.641$ Å is the lattice parameter of the virtual substrate $GaAs_{.94}P_{.06}$, and $\Lambda = 100$ Å. These values of σ and Λ are very close to the values frequently used for the GaAs-based THz QCLs.[10] The steady-state electron sheet densities for each of the subbands were found in an iterative manner where each iteration involved computing the average intersubband scattering rates and solving Eq. (146) in Ref. 10. We assumed T_e to be identical for all the subbands and incorporated the KEB method[10] in our simulation to take into account the difference between T_L and T_e.

In Table V, the calculated average electron scattering rates between relevant states of the
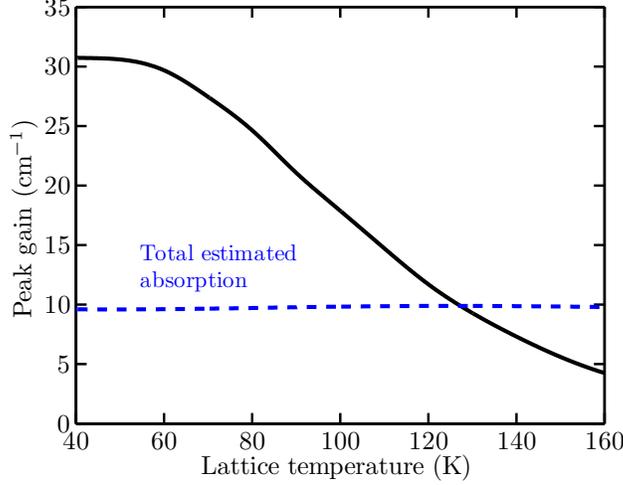
FIG. 5. Peak gain of the proposed THz QCL as a function of lattice temperature. The blue dashed line represents the total estimated loss.

designed structure and corresponding subband populations are presented. We calculated the unsaturated peak gain at different T_L, and the results are shown in Fig. 5. The gain spectrum was assumed to be Lorentzian, and the corresponding full-width at half-maximum was calculated by assuming the pure dephasing time as 0.33 ps.[42] The total loss, represented by the blue dashed line in Fig. 5, was supposed to be composed of two parts. The first part—waveguide loss considering the active region to be "lossless"—was taken from Ref. 43. We assumed that our structure employed Cu metal-metal waveguide for mode confinement. The second part—free carrier absorption due to the bound and quasi-bound Γ- and X_z-subbands—was estimated using the Eq. (34) of Ref. 44. From Fig. 5, we conclude that our designed THz QCL is capable of lasing up to a maximum T_L of ~125 K. Figure 6 shows J and unsaturated net gain as a function of applied bias for three different temperatures. We observe that the net gain peaks at 18 kV/cm and drops gradually past this bias at all three different temperatures. This happens because the state S3 almost perfectly aligns with S2 at 18 kV/cm, and the detuning of their alignment gradually increases as the bias increases beyond. We also find that negative-differential conductance phenomenon does not occur in the shown bias and temperature ranges.

Since the calculations of steady-state carrier densities and gain using the developed model are computationally demanding, we included the dominant Γ-valley states S1–S3 and X_z-valley states S4–S7 in the simulation results presented in Figs. 5 and 6. However, in reality,
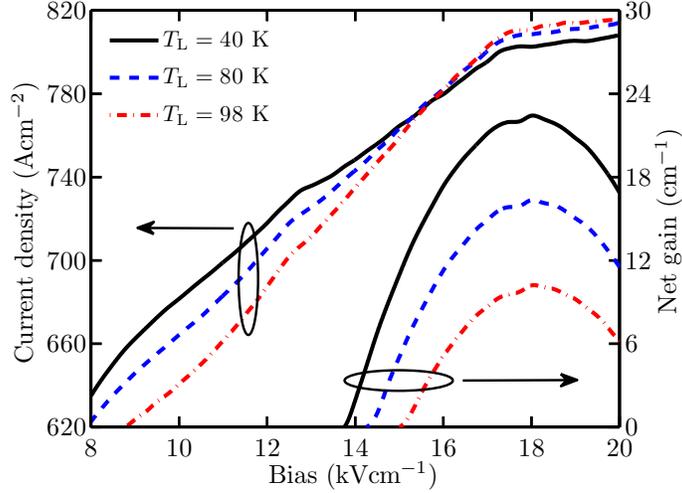
20

FIG. 6. Bias dependence of the current density and unsaturated net gain of the proposed THz QCL for three different lattice temperatures.

the scattering from these Γ- and X_z-valley states to other bound and quasi-bound Γ and X_z-valley states that are located at higher energies could be significant, especially at a higher temperature. Also, there could be carrier leakage to X_{xy}-valley states. Therefore, to calculate the gain at a more realistic case, we included one more Γ-valley state that has energy greater than S1–S3 and four more X_z-valley states that have energies greater than S4–S7. We also included carrier scattering to and from the X_{xy}-valley states. In particular, we included X_{xy}-X_{xy} Γ-point LO phonon, X_{xy}-X_{xy} X-point LA phonon, X_{xy}-X_{xy} intravalley IR, and X_{xy}-Γ and X_{xy}-X_z X-point LA phonon scattering mechanisms to the model already described. We calculated the gain using this extended model at 98 K and 130 K. We found that the gain dropped by $\sim$1.5 and $\sim$2 cm^{-1} at T_L of 98 and 130 K, respectively, with respect to that in Fig. 5. Since X_{xy}-states are doubly degenerate and are located lower in energy compared to other states that have higher energies than S1–S3 in Γ-valley and S4–S7 in X_z-valley, leakage of carriers to the X_{xy}-states is mainly responsible for the decrease of the gain calculated using the extended model. If the extended model with carrier leakages to higher energy Γ- and X_z-states and also to X_{xy}-states are taken into account, we estimate the maximum operating temperature for the proposed QCL to be $\sim$119 K.

For future improvement of our device, it is extremely important to identify the major performance-degrading factors. We identify three factors that we think are critical factors in deteriorating the performance of our designed THz QCL. The first factor is that the

average electron effective mass at the lasing subbands of our QCL ($\sim 0.09\,m_0$) is higher than that of the conventional GaAs/AlGaAs QCLs. As a result, gain coefficient decreases. The second factor is the not-so-fast IR assisted $X_z \rightarrow \Gamma$ carrier injection into the ULS and significant back-scattering from the Γ-valley ULS to the injector X_z-states. Although the carrier extraction rates from the LLS are relatively fast such as from S3 to S4 and S5, from S4 to S6 and S7, and from S5 to S6 and S7, the carrier injection rates to the ULS are relatively slow if we compare to QCL designs that employ only Γ-valley states in Ref. 45. The third factor is that the coupling between the states S1 and S3 is strong, which causes radiative leakage from S1 to S3, and thus decreases the peak gain. To maximize the gain of the proposed structure and thereby improve the current maximum operating temperature, an in-depth analysis of the influences of the various design variables on the device gain and current density needs to be performed.

V. CONCLUSION

We have designed a novel ~ 4.8 THz QCL that utilizes Γ-subbands for lasing transition and X_z-subbands as injector subbands. In our designed structure, carrier transition between the Γ- and X_z-states occurs predominantly through the **k**-non-conserving IR assisted scattering mechanism. We presented a model for the calculation of IR assisted intervalley electron transport. In the proposed structure, we introduced tensile strain at the injector region by using AlGaAsP, which helped to achieve substantial overlap between the Γ- and X_z-wavefunctions. The tensile strain also helped to push the ground X_{xy}-state considerably higher in energy than the ground injector X_z-state, and thus contributed importantly toward gain enhancement. We chose GaAs$_{.94}$P$_{.06}$ as the virtual substrate to essentially balance the strain over a period. We found that the maximum operating temperature reachable by our design was ~ 119 K. We identified three important factors responsible for the performance degradation. We believe that our proposed design, although has not demonstrated an excellent performance, will inspire researchers to explore novel intersubband devices that involve X-valley states in carrier dynamics.

REFERENCES

[1] R. Köhler, A. Tredicucci, F. Beltram, H. E. Beere, E. H. Linfield, A. G. Davies, D. A. Ritchie, R. C. Iotti, and F. Rossi, Nature **417**, 156 (2002).

[2] J. C. Cao, Sci. China Inf. Sci. **55**, 16 (2012).

[3] S. Fathololoumi, E. Dupont, C. Chan, Z. Wasilewski, S. Laframboise, D. Ban, A. Mátyás, C. Jirauschek, Q. Hu, and H. Liu, Opt. Express **20**, 3866 (2012).

[4] A. Wade, G. Fedorov, D. Smirnov, S. Kumar, B. S. Williams, Q. Hu, and J. L. Reno, Nat. Photonics **3**, 41 (2009).

[5] X. Gao, D. Botez, and I. Knezevic, J. Appl. Phys. **101**, 063101 (2007).

[6] C. Sirtori and R. Teissier, in *Intersubband Transitions in Quantum Structures*, edited by R. Paiella (McGraw-Hill, Inc., New York, 2006), p. 28.

[7] R. Teissier, J. J. Finley, M. S. Skolnick, J. W. Cockburn, J. L. Pelouard, R. Grey, G. Hill, M. A. Pate, and R. Planel, Phys. Rev. B **54**, R8329 (1996).

[8] J. J. Finley, R. J. Teissier, M. S. Skolnick, J. W. Cockburn, G. A. Roberts, R. Grey, G. Hill, M. A. Pate, and R. Planel, Phys. Rev. B **58**, 10619 (1998).

[9] G. Bastard, *Wave Mechanics Applied to Semiconductor Heterostructures* (EDP Science, Paris, 1992), p. 67.

[10] C. Jirauschek and T. Kubis, Appl. Phys. Rev. **1**, 011307 (2014).

[11] U. Frisch, *Turbulence: The Legacy of A. N. Kolmogorov* (Cambridge University Press, Cambridge, 1996), p. 44.

[12] D. H. Lenschow, V. Wulfmeyer, and C. Senff, J. Atmos. Ocean. Tech. **17**, 1330 (2000).

[13] J. M. Luttinger and W. Kohn, Phys. Rev. **97**, 869 (1955).

[14] See AIP Document No. E-PAPS: E-PRLTA-81-008827; available at `http://ftp.aip.org/epaps/phys_rev_lett`.

[15] J. B. Xia, Phys. Rev. B **41**, 3117 (1990).

[16] M. L. Cohen and T. K. Bergstresser, Phys. Rev. **141**, 789 (1966).

[17] S. R. Schmidt, E. A. Zibik, A. Seilmeier, L. E. Vorobjev, A. E. Zhukov, and U. M. Ustinov, Appl. Phys. Lett. **78**, 1261 (2001).

[18] R. People and J. C. Bean, Appl. Phys. Lett. **47**, 322 (1985).

[19] J. W. Matthews and A. E. Blakeslee, J. Cryst. Growth **27**, 118 (1974).

[20] P. J. Orders and B. F. Usher, Appl. Phys. Lett. **50**, 980 (1987).

[21] Y. C. Chen and P. K. Bhattacharya, J. Appl. Phys. **73**, 7389 (1993).

[22] P. Harrison, *Quantum Wells, Wires and Dots: Theoretical and Computational Physics*, 2nd ed. (Wiley, Chichester, 2005).

[23] I. Vurgaftman, J. R. Meyer, and L. R. Ram-Mohan, J. Appl. Phys. **89**, 5815 (2001).

[24] J. M. Smith, P. C. Klipstein, R. Grey and G. Hill, Phys. Rev. B **57**, 1740 (1998).

[25] H. Im, L. E. Bremme, P. C. Klipstein, A. V. Kornilov, H. Beere, D. Ritchie, R. Grey and G. Hill, Phys. Rev. B **70**, 205313 (2004).

[26] N. Miura, G. Kido, M. Suekane, and S. Chikazume, J. Phys. Soc. Jpn. **52**, 2838 (1983).

[27] S. Adachi, *Properties of Group-IV, III-V and II-VI Semiconductors* (Wiley, Chichester, 2005).

[28] H. Im, P. C. Klipstein, R. Grey and G. Hill, Phys. Rev. B **62**, 11076 (2000).

[29] "Gallium arsenide (GaAs) second- and third-order elastic moduli and compliances," in *Landolt-Börnstein - Group III Condensed Matter*, edited by O. Madelung, U. Rössler, and M. Schulz (Springer, Berlin, Heidelberg, 2001), Vol. 41A1α.

[30] D. Strauch, "AlP: elastic coefficients, internal strain parameter," in *Landolt-Börnstein - Group III Condensed Matter*, edited by U. Rössler (Springer, Berlin, Heidelberg, 2011), Vol. 44D.

[31] M. P. Semtsiv, O. Bierwagen, W. T. Masselink, M. Goiran, J. Galibert, and J. Léotin, Phys. Rev. B **77**, 165327 (2008).

[32] M. Oshikiri, K. Takehana, T. Asano, and G. Kido, J. Phys. Soc. Jpn. **65**, 2936 (1996).

[33] L. E. Bremme and P. C. Klipstein, Phys. Rev. B **66**, 235316 (2002).

[34] T. H. Glisson, J. R. Hauser, M. A. Littlejohn, and C. K. Williams, J. Electron. Mater. **7**, 1 (1978).

[35] J. Faist, F. Capasso, C. Sirtori, D. L. Sivco, and A. Y. Cho, in *Intersubband Transitions in Quantum Wells: Physics and Device Applications II*, edited by H. C. Liu and F. Capasso (Academic Press, New York, 2000), p. 06.

[36] S. Adachi, *Properties of Semiconductor Alloys: Group-IV, III-V and II-VI Semiconductors* (Wiley, Chichester, 2009), p. 106.

[37] G. Armelles, M. J. Sanjuán, L. González, and Y. González, Appl. Phys. Lett. **68**, 1805 (1996).

[38] D. Strauch and B. Dorner, J. Phys.: Condens. Matter **2**, 1457 (1990).

[39]P. H. Borcherds, K. Kunc, G. F. Alfrey, and R. L. Hall, J. Phys. C: Solid State Phys. **12**, 4699 (1979).

[40]S. Aouadi, P. Rodriguez-Hernandez, K. Kassali and A. Muñoz, Phys. Lett. A **372**, 5340 (2008).

[41]M. Lundstrom, *Fundamentals of Carrier Transport*, 2nd ed. (Cambridge University Press, Cambridge, 2000), p. 115.

[42]S. Kumar, Ph.D. thesis, Massachusetts Institute of Technology, 2007.

[43]M. A. Belkin, J. A. Fan, S. Hormoz, F. Capasso, S. P. Khanna, M. Lachab, A. G. Davies, and E. H. Linfield, Opt. Express **16**, 3242 (2008).

[44]C. Ndebeka-Bandou, F. Carosella, R. Ferreira, A. Wacker, and G Bastard, Semicond. Sci. Technol. **29**, 023001 (2014).

[45]E. Dupont, S. Fathololoumi, Z. R. Wasilewski, G. Aers, S. R. Laframboise, M. Lindskog, S. G. Razavipour, A. Wacker, D. Ban, and H. C. Liu, J. Appl. Phys. **111**, 073111 (2012).